

pubs.acs.org/JPCC Article

Influence of Electronic Configurations on the Modulation of Fermi/ Orbital Junction Energies for Directional Electron Transport through 3d¹, 3d³, and 3d⁵ Metallosurfactants

A. D. K. Isuri Weeraratne, Neha Rani, Samudra Amunugama, S. Sameera Perera, Kenneth K. Kpogo, Shivnath Mazumder, and Cláudio N. Verani*



ACCESS I

Cite This: J. Phys. Chem. C 2022, 126, 21010–21021

III Metrics & More



Article Recommendations

 O_{SOMO} biased Au₁ Au₂ biased Au₂ Au₁ O_{SOMO} O_{S

ABSTRACT: Two new metallosurfactants containing the $3d^1$ vanadyl(IV) and $3d^3$ chromium(III) ions bound to the phenylenediamine-bridged phenolate-rich ligand $L^{N_2O_2}$ were designed, deposited as monolayer films on gold electrodes, and probed for directional electron transfer in AulLBlAu junctions. Both $[V=O^{IV}L^{N_2O_2}]$ (1) and $[Cr^{III}(L^{N_2O_2})(MeOH)(H_2O)]Cl$ (2) promote current rectification. Through a concerted experimental and computational effort, we compare the behavior of 1 and 2 with that of our previously studied $3d^5$ $[Fe^{III}(L^{N_2O_2})Cl]$ (3). Based on the analysis of comprehensive electrochemical, spectroscopic, and microscopy results allied to DFT calculations, we propose distinct mechanisms by which electronic configurations influence the energy gap between the electrode Fermi levels and the different molecular orbitals responsible for electron transport. While the $3d^5$ species 3 shows electron transport through the metal-based SOMO located above the Fermi levels of the electrode, the $3d^1$ species 1 uses a metal-based SOMO below Fermi, and the $3d^3$ species 2 takes advantage of a ligand-based HOMO, which becomes available when a bias is applied.

■ INTRODUCTION

The theoretical model proposed by Aviram and Ratner¹ for unimolecular rectification, or directional electron transport via through-bond tunneling, involves the placement of a molecule containing σ -bridged donor and acceptor moieties between two electrodes. As originally proposed, this $E_1|D-\sigma-A|E_2$ molecular junction requires an excited state $[D^+-\sigma-A^-]$ of higher but accessible energy generated by the transfer of one electron from the electrode E2 to the LUMO of the acceptor, $A^{LUMO} \leftarrow E_2$. Simultaneously another electron is transferred via $E_1 \leftarrow D^{HOMO}$. The excited electron in A^{LUMO} then relaxes to \overline{D}^{HOMO} replenishing the $[D\text{-}\sigma\text{-}A]$ state. The experimental verification of this I/V response was attained experimentally using a synthetically accessible π -bridged species $^{2-5}$ and has been continuously expanded ever since. New molecules based on electron transfer using energy mismatch between two conducting levels of the molecule, e.g., $A^{\rm LUMO}$ and $D^{\rm LUMO}$, were developed,6 and soon thereafter, molecules able to promote

asymmetric rectification exclusively through the LUMO⁷ or the HOMO⁸ were proposed. Recently, we observed rectification in AulLBlAu junctions containing Langmuir—Blodgett (LB) monolayers of metallosurfactants, a new class of amphiphilic compounds containing a five-coordinate high-spin Fe^{III} ion (3d⁵, S = 5/2). Unlike in previous systems based on LUMO and HOMO tunneling, electron transport took place through the metal-based SOMOs ($d_{xz} + d_{yz}$) when they were within 1 eV from the Fermi level of the electrodes. ^{9,10} When the energy of the SOMOs was mismatched with that of the Fermi levels of the electrode, *e.g.*, in Cu^{II} surfactants in which a

Supporting Information

Received: July 8, 2022
Revised: November 8, 2022
Published: November 23, 2022





Scheme 1. 3d¹, 3d³, and 3d⁵ Metallosurfactants

 $3d^9$ configuration leaves the highest $3d_{x2-y2}$ as the only singly occupied MO, an insulating behavior was observed. These results were validated statistically 11,12 and permitted us to postulate that for some systems containing transition metals, the SOMOs rather than the LUMOs are the operative orbitals for tunneling. The semioccupied nature of these orbitals may limit the amplitude of the current response due to spin restrictions imposed by Pauli's exclusion; however, this property may be advantageous for spin transport research in electronic materials. ^{13,14} Accordingly, the formation of a radical in an initially closed-shell organic species leads to SOMO transport, 15 while HOMO rectification is observed in organometallic species such as ferrocene. 16 However, radical formation within a triphenyl acceptor near a ferrocene species hampers rectification even when bringing the organic SOMO within the bias window. Other examples of SOMO/ HOMO interplay have been reported by manipulating changes from the high-spin S = 5/2 to the low-spin S = 1/2 state in Mn²⁺ and Fe³⁺ species, either by electrical¹⁸ or thermal¹⁹ stimuli. In both cases, the HS state enables tunneling through the SOMOs and precludes it when a LS state with fully occupied HOMOs is operative. In spite of remarkable progress, the influence of electronic configurations on the mechanism of directional electron transport is neither well understood nor systematically assessed. We hypothesize that, within first-row metals, a specific number of electrons in the metal center of the metallosurfactant in the AulLBlAu junction will lead to distinct molecular orbital energies that determine the alignment of the Fermi levels of the electrodes with the LUMO, SOMO, or HOMO levels of the molecule. In this study, we analyze the rectification response of two new systems shown in Scheme 1, the $3d^1$ [V= $O^{\overline{1}V}L^{N_2O_2}$] (1) with a doublet (S = 1/2) structure (S = 3/2) structure, and compare these $3d^1$ and $3d^3$ species with our previously studied $3d^{\tilde{5}}$ [Fe^{III}(L^{N₂O₂})Cl] (3)¹⁰ (sextet, S = 5/2).

We offer a detailed study involving multiple experimental methods such as UV—visible, infrared (IR), IR reflectance/absorbance (IRRAS), X-ray and UV photoelectron spectroscopies (XPS, UPS), cyclic voltammetry (CV), and current/voltage (I/V) responses, allied to DFT calculations to propose a description of through-SOMO and through-HOMO transport, including a discussion on how the currents and rectification ratios get affected.

EXPERIMENTAL SECTION

Materials and Methods. Reagents and solvents were purchased from commercial sources and used without further purification. ¹H-NMR spectra were recorded using a Varian 400 MHz instrument using CDCl₃ or CD₃CN as the solvent.

Chemical shifts (δ) are given in ppm and coupling constants (J) in Hertz (Hz). Elemental analyses were performed by Midwest Microlab, Indianapolis, Indiana. Infrared spectra were measured in the range from 4000 to 600 cm⁻¹ as KBr pellets on a Tensor 27 FTIR spectrophotometer, and 64 scans were used to obtain the IR spectra of the compounds.

A Bruker Tensor 27 infrared spectrophotometer outfitted with an A513/Q variable-angle accessory was used to perform the infrared reflection absorption (IRRAS) spectra of the LB films. Five-minute scanning time was used for each IRRAS spectrum. ESI spectra were measured using a triple quadrupole Micromass Quattro LC instrument. UV-visible spectra were measured in the range from 200 to 1100 nm on a SHIMADZU UV-3600 spectrophotometer. Electrochemical experiments were carried out on a BAS 50W voltammetric analyzer. A standard three-electrode cell was used with a glassy-carbon working electrode, Pt-wire auxiliary electrode, and Ag/AgCl reference under an inert atmosphere at room temperature. Tetrabutylammonium hexafluorophosphate was used as the supporting electrolyte, and the scans were run at 100 mV/s. Ferrocene was used as the internal standard, and all the potential values were referred to versus the Fc+/Fc couple.

Synthesis of Ligand [H₂L^{N₂O₂]. The ligand was synthesized as previously described, where a methanol solution of 4,5-bis(2-methoxyethoxy)benzene-1,2-diamine (1.0 g, 4.3 mmol) was added dropwise to a stirred mixture of 3,5-ditert-butyl-2-hydroxybenzaldehyde (2.0 g, 8.5 mmol) in methanol and refluxed for 18 h under an inert atmosphere. The dark orange turbid solution was stored at 4 °C overnight and filtered to yield a dark orange microcrystalline solid, which was washed with cold methanol and dried under vacuum. Yield: 78%. ESI (m/z^+) in $CH_2Cl_2 = 689.4525$ for $[C_{42}H_{60}N_2O_6 + H^+]$. H NMR, ppm (CDCl₃, 400 MHz): δ 1.305–1.453 (m, 36H^{fBu}), 3.459 (s, 6H^{OCH₃}), 3.794 (t, 4H^{OCH₂}), 4.236 (t, 4H^{OCH₂}), 6.884 (s, 2H^{ph}), 7.196 (d, 2H^{ph}), 7.411 (d, 2H^{ph}), and 8.635 (s, 2H^{CH}). IR (KBr, cm⁻¹): 3245 (ν_{O-H}) , 2811–2957 (ν_{C-H}) , 1616 $(\nu_{C=C})$ aromatic), 1511 $(\nu_{C=C})$, aromatic), 1578 $(\nu_{C=N})$, 1266 (ν_{C-O-C}) , and 1129 (ν_{C-O-C}) .}

Synthesis of the Metallosurfactants 1 and 2. [$V = O^N L^{N_2O_2}$] (1). A solution containing $H_2 L^{N_2O_2}$ (0.600 g, 0.870 mmol) in methanol (15 mL) was treated with methanolic vanadyl acetylacetonate (0.276 g, 1.04 mmol). The reaction mixture was refluxed with stirring for 4 h, and the solvent was evaporated to 1/5 of the original volume and kept in the refrigerator for 48 h prior to filtration. The filtrate was washed with n-hexane to yield greenish crystals. Yield = 63%. HD-ESIMS+ (m/z) in CH₃OH = 754.0135 [$C_{42}H_{58}VV_2O_7 + H^+$]⁺. Anal. calc for [$C_{42}H_{58}V_2O_7V$]: C, 66.92; H, 7.76; and N, 3.72%. Found: C, 67.08; H, 7.74; and N, 3.82%. IR (KBr,

cm⁻¹): 2850–2970 ($\nu_{\rm C-H}$), 1608 ($\nu_{\rm C=C}$, aromatic), 1507 ($\nu_{\rm C=C}$, aromatic), 1590 ($\nu_{\rm C=N}$), 1253 ($\nu_{\rm C-O-C}$), and 1112 ($\nu_{\rm C-O-C}$).

 $[Cr^{\parallel \parallel}(L^{N_2O_2})(MeOH)(H_2O)]Cl$ (2). Complex 2 was synthesized by treating an anhydrous tetrahydrofuran solution of H₂L^{N₂O₂} (0.100 g, 0.145 mmol) with anhydrous CrCl₂ (0.021 g, 0.174 mmol). The resulting dark brown solution was stirred under argon for 18 h and then kept open to air for 6 h. The reaction mixture was then diluted with diethyl ether and washed with aqueous saturated NH₄Cl (3 \times 150 mL) and brine solution (3 × 150 mL). The organic phase was dried with Na₂SO₄, and the solvent was removed under reduced pressure. The resulting product was recrystallized in methanol:dichloromethane (3:1) to yield dark brown crystals. Yield: 80%. HD-ESIMS+ (m/z) in $CH_3OH = 802.1347$ for $[C_{44}H_{66}N_2O_8Cr]^+$. Anal. calc for [C₄₃H₆₄ClCrN₂O₈]: C, 62.65; H, 7.82; and N, 3.40% Found: C, 62.87; H, 8.02; and N, 3.34%. IR (KBr, cm⁻¹): 2851-2920 (ν_{C-H}) , 1610 $(\nu_{C=C, \text{ aromatic}})$, 1509 $(\nu_{C=C, \text{ aromatic}})$, 1588 $(\nu_{\rm C=N})$, 1263 $(\nu_{\rm C-O-C})$, and 1121 $(\nu_{\rm C-O-C})$.

X-ray Structural Determination of Metallosurfactant 2. Diffraction data for [Cr^{III}(L^{N₂O₂})(MeOH)(H₂O)]Cl (2) was measured on a Bruker X8 APEX-II²⁰ kappa geometry diffractometer with Mo radiation and a graphite monochromator. Single crystals of 2 were metallic brown. A suitable crystal was selected and mounted on the Bruker APEX-II CCD diffractometer. Frames were collected at 100.1 K with the detector at 40 mm and 0.3° between each frame and were recorded for 15 s. A total of 42,448 reflections were collected, with 4162 independent reflections ($R_{int} = 0.0482$). Using Olex2,²¹ the structure was solved with the olex2.solve² structure solution program using Charge Flipping and refined with the XL²³ refinement package using least squares minimization. Hydrogen atoms were placed in calculated positions. The asymmetric unit contained one complex coordinated to water, and methanol molecules axially, one uncoordinated methanol solvate and a chloride counter ion. All crystallographic parameters of 2 are shown in Table S1

Compression Isotherms. The surface pressure (Π) *versus* average molecular area (A) isotherms were examined using an automated KSF Minitrough at (22.8 ± 0.5) °C. Ultrapure water with a resistivity of 17.5–18 M Ω /cm was obtained from a Barnstead NANOpure system and used in all experiments. Impurities present at the surface of the freshly poured aqueous subphase were removed by vacuum after compression of the barriers. Spreading solutions were prepared in spectroscopygrade chloroform. A known quantity (typically 25 mL) of freshly prepared surfactant solution with a known concentration (1 mg/mL) was then spread on the clean aqueous subphase. The system was allowed to equilibrate for approximately 10 min before compression. The Π versus A isotherms were obtained at a compression rate of 10 mm/min. The Wilhelmy plate method (paper plates, 40 mm diameter) was used to measure the pressure. At least three independent measurements were carried out per sample, with excellent reproducibility attained.

Brewster Angle Microscopy. A KSV-Optrel BAM 300 equipped with a HeNe laser (10 mW, 632.8 nm) and a CCD detector was used for all micrographs. The compression rate was 10 mm/min, the field of view was 800 μ m × 600 μ m, and the lateral resolution was about 2–4 μ m.

X-ray Photoelectron Spectroscopy. A Thermo Scientific Nexsa X-ray photoelectron spectrometer (XPS) with a hemispherical analyzer and monochromatic Al $K\alpha$ source

was used to analyze both the powdered samples and the deposited LB films of the complexes. The samples were mounted on a standard holder using Cu-spring clips. Then, the sample holder was loaded into the entry lock and held under vacuum ($<5 \times 10^{-7}$ mbar) for ~ 30 min. Once the pressure in the entry-lock chamber reached $\sim 4 \times 10^{-7}$ mbar, the sample holder was transferred to the analysis chamber, which was kept at a base pressure $\sim 1.8 \times 10^{-7}$ mbar during data acquisition. High-resolution spectra were collected using 50 eV passenergy, 0.1 eV energy step size, and 100 ms/step dwell time. Recorded spectra were analyzed using Thermo Avantage v5.9922 software to extract qualitative information. The C 1s, V 2p, and Cr 2p peaks were fitted using Voight functions (Gaussian 65% and Lorentzian 30%).

Ultraviolet Photoelectron Spectroscopy. LB films were characterized using a Thermo Scientific Nexsa X-ray photoelectron spectrometer (XPS) equipped with UPS capabilities. UPS experiments were performed with the He I (21.22 eV) photon lines from a He-discharge lamp. Samples were mounted on a UPS bias sample holder using Cu-spring clips and handled in a similar way as described for XPS. Once the pressure in the entry-lock chamber reached $\sim 4 \times 10^{-7}$ mbar, the sample holder was transferred to the analysis chamber, which was kept at a base pressure of $\sim 3.6 \times 10^{-7}$ mbar for data acquisition. A $\sim 10^{-7}$ V bias was applied to overcome the difference in work function between the analyzer and the sample. The high-resolution UPS spectra were recorded using 2 eV pass-energy, 0.05 eV energy step size, and 150 ms/step dwell time. Spectra were analyzed using Thermo Avantage

Computational Methods. All of the calculations were performed using density functional theory $(\mathrm{DFT})^{24}$ with Gaussian 09, 25 using $\mathrm{B3LYP}^{26,27}$ functional with SDD basis set and pseudopotentials $^{28-30}$ on iron, vanadium, and chromium, and $6-31\mathrm{G}(\mathrm{d,p})$ basis 31,32 on the other atoms. To reduce the computational cost, a slightly modified model was used where the methoxyethoxy substituents of the phenylenediamine moiety were replaced by methoxy groups. All optimized structures were confirmed as minima by analyzing the harmonic vibrational frequencies. Solvation effects (in dichloromethane) were accounted for using the implicit SMD continuum solvation model and were included during structure optimization. Isodensity plots of orbitals and spin densities were visualized using GaussView. 34

■ RESULTS AND DISCUSSION

Synthesis and Characterizations. The ligand $[H_2L^{N_2O_2}]$ is 6.6'-((1E,1'E)-((4.5-bis(2-methoxyethoxy)-1.2-phenylene)bis(azaneylylidene))bis(methaneylylidene))bis(2,4-di-tert-butylphenol) and was synthesized as previously published.^{9,10} The metallosurfactants $[V=O^{IV}L^{N_2O_2}]$ (1) and $[Cr^{III}(L^{N_2O_2})]$ (MeOH)(H₂O)]Cl (2) were obtained by treating 1 equiv of the ligand, respectively, with VO(acac)₂ or CrCl₂. 35,36 The FTIR spectra for 1 and 2 showed symmetric and asymmetric C-H stretching vibrations in the range of 2840-2970 cm⁻¹ and a prominent peak at 1588 cm⁻¹ for C=N stretching vibrations. Elemental analysis for 1 and 2 showed a good correlation between experimental and theoretical values and HD-ESIMS confirmed peaks at m/z = 754.0135 for 1 and m/z= 802.1347 for 2. X-ray quality brown single crystals were obtained for $[Cr^{III}(L^{N_2O_2})(MeOH)(H_2O)]Cl$ (2) from a methanol/dichloromethane (3:1) solvent mixture. The crystal structure shown in Figure 1 and Table S1 reveals a six-

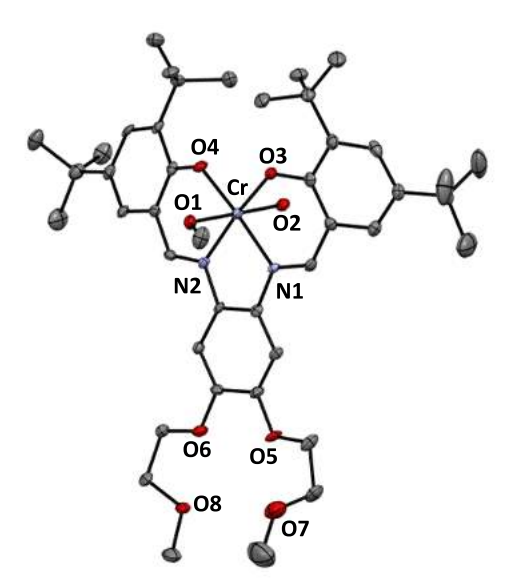


Figure 1. ORTEP representation at 50% probability for 2 (CCDC 2096599). H atoms omitted for clarity.

coordinate pseudo-octahedral geometry in which the metal center is coordinated at the basal plane by two imine nitrogen and two phenolate oxygen atoms of the ligand $L^{N_2O_2}$, with water, and methanol at the axial positions. The amine and phenolate donors are *trans* to each other, with Cr-O and Cr-N average bond lengths at 1.902 and 2.004 Å, respectively. These distances are comparable to other data reported for similar Cr^{III} complexes.³⁷ Attempts to grow X-ray quality single crystals for the vanadyl analogue 1 were unsuccessful.

Electronic and Redox Behavior. The UV–visible spectra are dominated by ligand-to-ligand and ligand-to-metal charge transfer bands (See Figure S1 along with discussion). The redox response for both the vanadyl and the chromium species 1 and 2 shows a process at anodic current (Figures 2 and S2). For 1, this process is observed at 0.09 $V_{Fc+/Fc}$ ($\Delta E_p = 0.17 \text{ V}$, | I_{pa}/I_{pc} | = 1.16), whereas for 2, this process appears at 0.31 $V_{Fc+/Fc}$ ($\Delta E_p = 0.12 \text{ V}$, | I_{pa}/I_{pc} | = 1.11). These electrochemical events were further investigated using DFT methods²⁴ to obtain the spin-density plots with Mulliken spin density (MSD) values on the metal centers of the relevant species. Species 1 is a doublet with a MSD value of 1.11 on the metal center illustrating the presence of the V^{IV} metal with a 3d¹

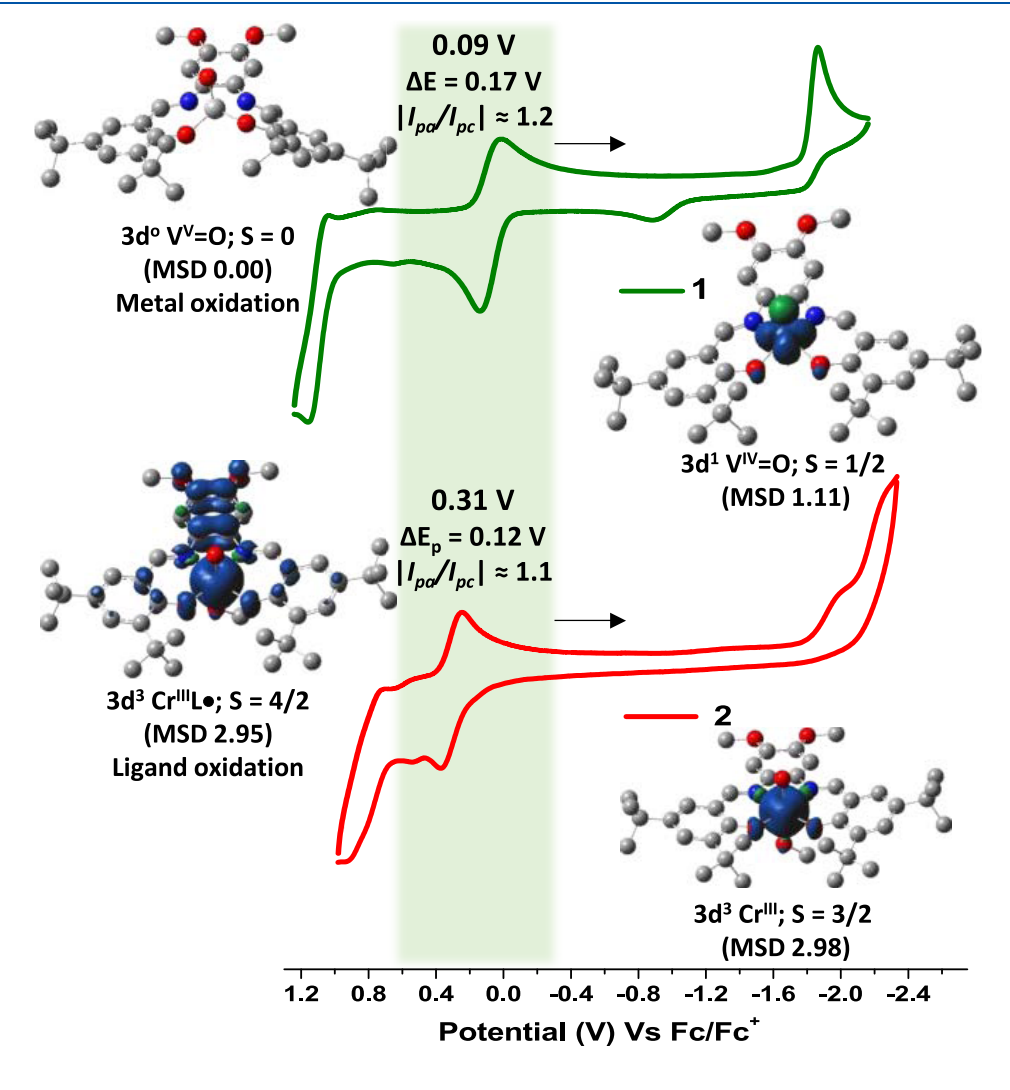


Figure 2. Cyclic voltammograms for 1 and 2 using glassy carbon (WE), Ag/AgCl (RE), Pt wire (AE), and TBAPF₆. Potentials *versus* the Fc⁺/Fc couple. The relevant DFT-calculated spin-density plots for before and after 1e⁻ oxidation of these species (isodensity 0.004 a.u.) are shown with Mulliken spin density (MSD) values on the metal centers.

electronic configuration. The 1 e- oxidation of 1 was confirmed to be a metal-based process described as 3d1 $(V^{IV}=O)^{2+}$ to $3d^0$ $(V^V=O)^{3+}$. The chromium-containing metallosurfactant 2 shows a quartet ground state. The MSD value on the metal center is 2.98 confirming the presence of a $3d^3$ Cr^{III} ion. Oxidation of 2 leads to the formation of 2^+ having a high-spin quintet configuration. The MSD value on Cr in 2⁺ is calculated to be 2.95, indicating that the Cr^{III} state is preserved after oxidation. Therefore, the oxidation of 2 is ligand-based, i.e., 3d³ [CrIIIL]+ to 3d³ [CrIIIL•]²+, giving rise to a radical delocalized over the phenylenediamine moiety. 10 These results are in good agreement with the behavior observed for the $3d^5$ Fe III species 3, which shows the phenylenediamine oxidation at $0.64 \text{ V}_{\text{Fc+/Fc}}$ ($\Delta E_p = 0.12 \text{ V}$, | $I_{\rm pa}/I_{\rm pc}$ || = 1.08). As we discussed previously, ¹⁰ the oxidation loci for 1+, 2+, and 3+ differ from the expected oxidation centered on the phenolate groups seen for the rectifying $[N_2O_3]$ iron(III) complex. 9 This is consistent with results presented by Thomas and co-workers, which working with ligands similar to LN2O2 presented here, propose phenylenediamine oxidation based on EPR data.^{38,3}

A second quasi-reversible oxidation is observed for all three species at about 1.0 $V_{Fc+/Fc}$ and involves a phenolate/phenoxyl couple. It is less relevant to this discussion because the process, when estimated in eV (see eqs 1 and 2 in Feasibility and Verification of Electron Transport), is energetically mismatched with the Au Fermi levels (Figure 2). Unlike species 3, which shows a reversible reduction at $-1.02~V_{Fc+/Fc}~(\Delta E_p=0.12~V,~|I_{pa}/I_{pc}|=0.93)$ assigned to the 3d $^5~Fe^{III}$ to 3d $^6~Fe^{II}$ redox process, the chromium-containing 2 displays an ill-formed process at $ca.~-2.~0~V_{Fc+/Fc}$ associated with chemical irreversibility. The vanadyl-bearing 1 shows a better-defined, but irreversible, reduction process at $-1.88~V_{Fc/Fc+}$ associated with the nominal $V^{IV} = O/V^{III} = O~(3d^1/3d^2)$ couple. This behavior is complex in nature, but well documented, 40 and attributed to the fast protonation of the $V^{III} = O~moiety$.

Interfacial Behavior and Film Formation. The interfacial properties of air | water Pockels-Langmuir 41a-d and air | solid Langmuir-Blodgett films of species 1 and 2 were evaluated to enable the design and preparation of monolayers on gold electrodes for AulLBlAu junctions (Figure 3). Isothermal compression and Brewster angle microscopy (BAM) were used at 25 °C to assess the average area per molecule, the collapse pressure of the monolayers, and the film topology. Good amphiphilicity supported by the hydrophobic tert-butyl groups and the hydrophilic alkoxy chains was observed and isothermal compression led to intermolecular interactions, at 81 and 85 Å²/molecule for metallosurfactants 1 and 2, respectively. Further compression led to the formation of homogeneous films, as confirmed by BAM images and to a slow constant-pressure 42,43 collapse after 40 mN/m with critical areas extrapolated at 77 and 79 Å²/molecule for 1 and 2, respectively. This behavior is consistent with that reported for 3,10 in which interaction appears at 74 Å2/molecule, and collapse at 40 m/Nm, with a critical area of 71 Å²/molecule. The vanadyl 1 is structurally closer to 3 as both species are 5coordinate. The marginally larger areas observed for 2 are tentatively attributed to its pseudo-octahedral geometry.

The molecular composition of the films was confirmed by UV-visible and infrared reflection absorption spectroscopy (IRRAS) spectroscopies. Although all our AulLBlAu junctions contain a single monolayer, the IRRAS measurements require the accumulation of 40 monolayers on each side of a glass

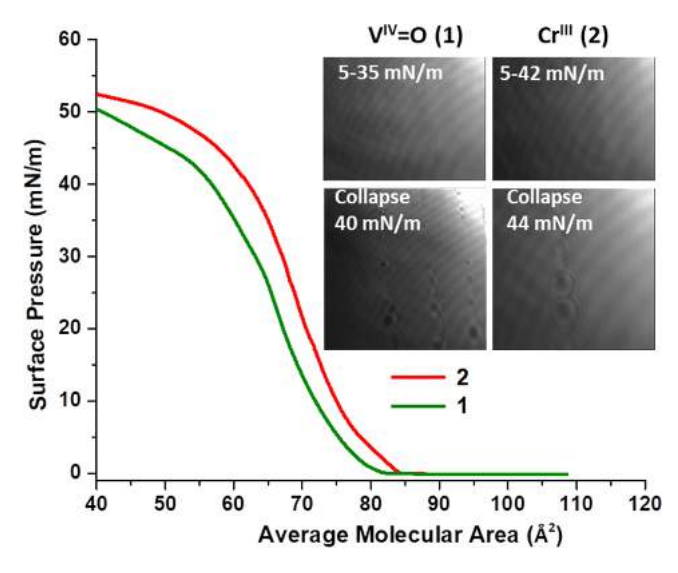


Figure 3. Compression isotherms for 1 and 2 with selected BAM micrographs showing films during compression and collapse.

substrate for verification of the composition. ⁴⁴ The UV-visible spectrum of LB 2 correlates well with the solution spectrum (Figures S1 and S3) and maintains the characteristic LMCT bands. Minor shifts are due to conformational changes during deposition.

The IRRAS spectra for LB 1 and 2 were compared to the FT-IR of the bulk samples. The LB spectra showed peaks due to aromatic C=C stretching between 1610 and 1500 cm⁻¹ and angular CH_2 and CH_3 deformations in the 1359–1500 cm⁻¹ region. The characteristic C=N stretching vibrations observed around 1585 cm⁻¹ correlate well with the bulk IR spectrum (Figures 4 and S4–S6). The characteristic stretch

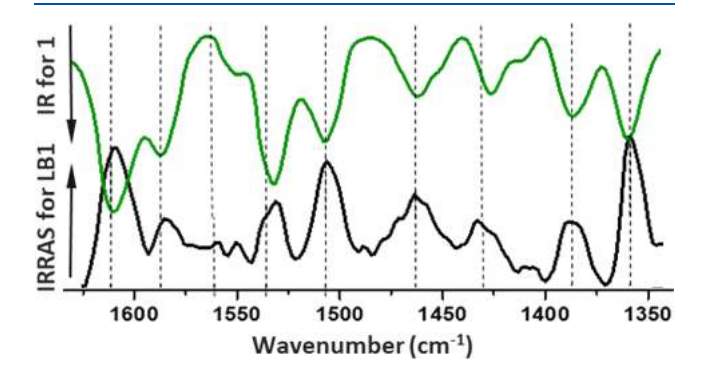


Figure 4. Comparative IR (bulk) and IRRAS (LB) for the vanadyl-containing ${\bf 1}.$

mode of the V=O group in 1 appeared at 977 cm⁻¹, but detection of this peak in LB films is challenging due to IRRAS surface selection rules, in which the V=O dipole moment is perpendicular to the electric field of the polarized light. This absence could be erroneously interpreted as vanadyl decomposition and to confirm the chemical composition of 1, we scraped off and dissolved the deposited film in MeOH and measured the mass spectrum; as expected, a peak at m/z = 754.27 was observed, confirming the presence of the V=O group (Figure S7).

The morphology of the LB monolayers 1 and 2 was probed by AFM at deposited surface pressures of 15, 20, 25 (27 for 1), and 35 mN/m (Figures S8 and S9). Monolayers deposited at

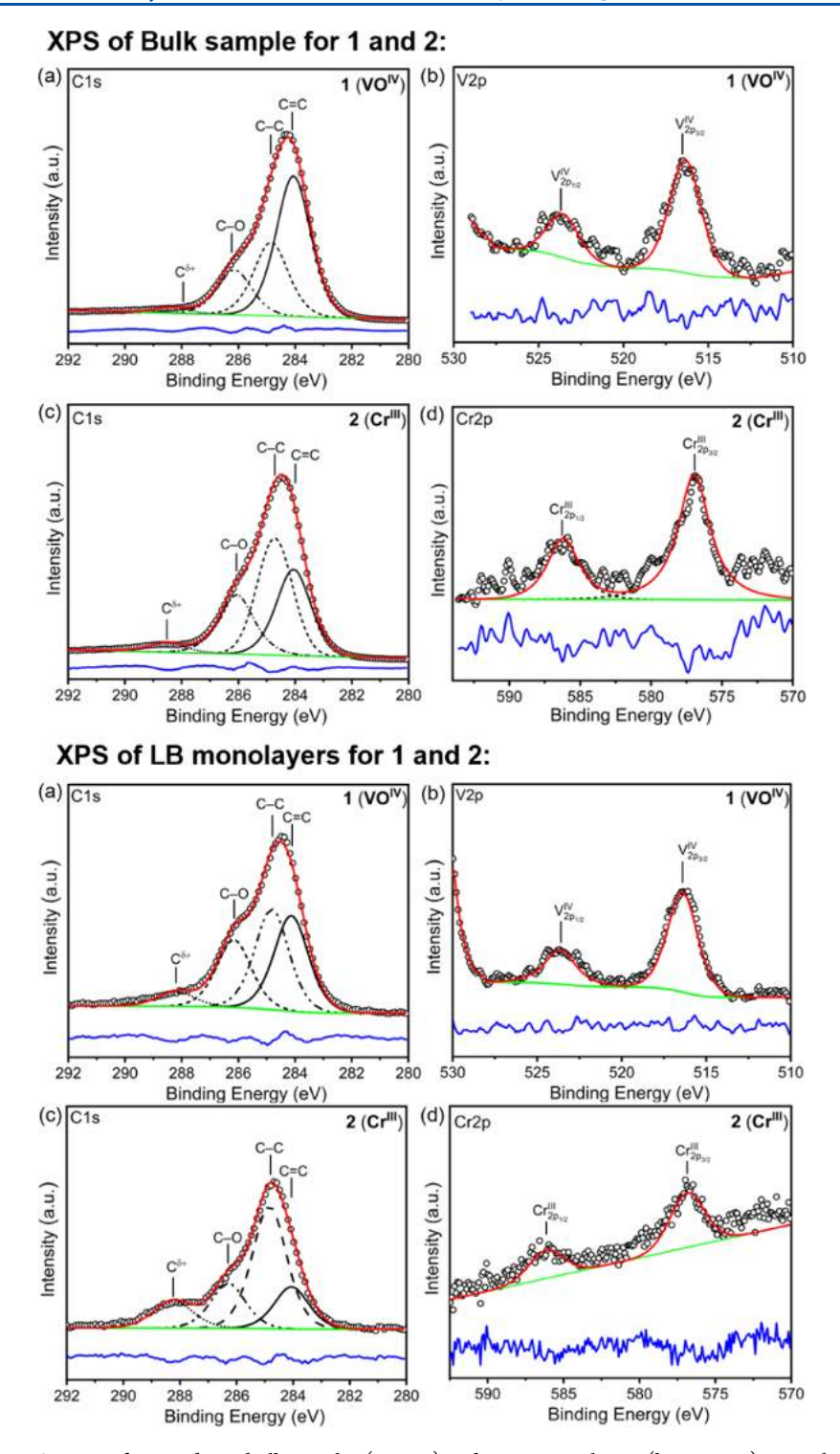


Figure 5. High-resolution XPS spectra for 1 and 2 as bulk samples (top set) and as LB monolayers (bottom set). In each set: (a) C 1s spectrum for 1; (b) V 2p spectrum for 1; (c) C 1s spectrum for 2; and (d) Cr 2p spectrum for 2. All spectra show experimental data (O), calculated fits (—), background (—), and residual (—) traces.

lower surface pressures show a high incidence of pinhole defects, and those at higher surface pressures show rougher surfaces due to aggregation. Films deposited at 20 mN/m for 1 and 25 mN/m for 2 show the best morphology for the assembly of $Au_1 ILBIAu_2$ junctions.

Retained Composition of the LB Films. The $3d^1$ and $3d^3$ metallosurfactants $[V=O^{IV}L^{N_2O_2}]$ (1) and $[Cr^{III}(L^{N_2O_2})-(MeOH)(H_2O)]Cl$ (2) were analyzed using X-ray photo-

electron spectroscopy, XPS, as bulk solid samples (Figure 5, top) and as LB films deposited on gold (Figure 5, bottom), to interrogate whether the identity of these species is preserved upon transfer. The high-resolution C 1s and V 2p/Cr 2p spectra recorded for the V^{IV}=O species 1 are described in Figure 5, top, a,b as peak fits for the C1s and V2p spectra, respectively. The C1s spectrum was deconvoluted in four peaks centered at 284.0, 284.8, 286.1, and 288.3 eV,

respectively. These peaks are assigned to the C=C, C-C, and C—O environments expected in a ligand containing phenolate rings and electron-poor carbon atoms.⁴⁷ The V 2p spectrum exhibited two peaks centered at 516.3 (V 2p_{3/2}) and 523.7 (V $2p_{1/2}$) eV confirming the presence of coordinated V^{IV}=O ions. 48 Similarly, Figure 5, top, c,d shows the C1s and Cr2p spectra for the bulk CrIII species 2. The C1s spectrum was deconvoluted into four peaks, and the binding energies were almost identical to those of the V^{IV}=O counterpart 1. The Cr $2p_{3/2}$ and Cr $2p_{1/2}$ peaks centered at 576.9 and 586.2 eV, respectively, were unambiguously assigned to a Cr^{III} species.⁴⁹ Figure 5, bottom, shows the high-resolution C1s, V2p, and Cr2p spectra recorded for the LB films of 1 and 2, respectively. Figure 5, bottom, a,b shows the fitted peaks to the C1s and V2p spectra recorded for the LB film of 1. Similar to the spectra of the powdered sample, the C=C, C-C, and C-O, and electron-poor carbon environments in the C1s spectrum show four peaks centered at 284.1, 284.8, 286.2, and 288.2 eV, respectively. The two peaks centered at 516.40 (V 2p_{3/2}) and 523.9 (V $2p_{1/2}$) eV in the V2p spectrum confirm the presence of V^{IV} in the film. Figure 5, bottom, c,d shows the C1s and Cr2p spectra recorded for the LB film of 2. The C1s spectrum displays identical characteristics to its V^{IV}=O LB counterpart, with similar binding energy values. The peaks centered at 576.8 and 586.1 eV were assigned to Cr $2p_{3/2}$ and Cr $2p_{1/2}$. These results confirm that the characteristics of metallosurfactants 1 and 2 as bulk solids were preserved after deposition as LB films.

Fabrication of $Au_1 | LB | Au_2$ Junctions. High-quality monolayers of the $V^{IV}O$ -containing 1 and Cr^{III} -containing 2 were deposited, respectively, at 20 and 25 mN/m on a precleaned gold substrate (Au_1 , bottom) and dried in a desiccator for 5 days under reduced pressure. The top gold electrode (Au_2) was deposited using shadow masking 50 with an Effa-Coater gold sputter. Three assemblies containing 16 individual $Au_1 | LB | Au_2$ junctions were prepared for each metallosurfactant, yielding a total of 48 junctions for 1 and 48 junctions for 2 to be analyzed for their current—voltage (I/V) characteristics using a Keithley 4200 semiconductor parameter analyzer and a Signatone S-1160 probe station at ambient conditions.

Current–Voltage Responses. Molecules in $\mathrm{Au_1}|\mathrm{LB}|\mathrm{Au_2}$ junctions can yield one of three distinct I/V responses: 51 (i) the molecules may act as insulators and no current is transported, as indicated by a flat line, (ii) the molecules may act as conductors, and a sigmoidal curve indicates that current is transported bidirectionally between electrodes, or (iii) the molecules may act as rectifiers, thus yielding an asymmetric curve with a sharp response to negative potentials, followed by a negligible response from positive potential (or vice-versa). The latter response is observed for 1 and 2, as indicated in Figure 6.

The reproducibility of the I/V curves was probed by measuring the response of several junctions of a given assembly, as well as by measuring different assemblies (Figures S10 and S11). Among each assembly, ca. 11–12 junctions were short-circuited due to monolayer defects, and an average of 25–30% of junctions showed clear rectification behavior for both 1 and 2. This distribution is expected for such junctions^{9,10} and the rectification can be quantified by their rectification ratio⁵ (RR = $[I \text{ at } -V_o/I \text{ at } +V_o)]$ and the amplitude of the current signal.

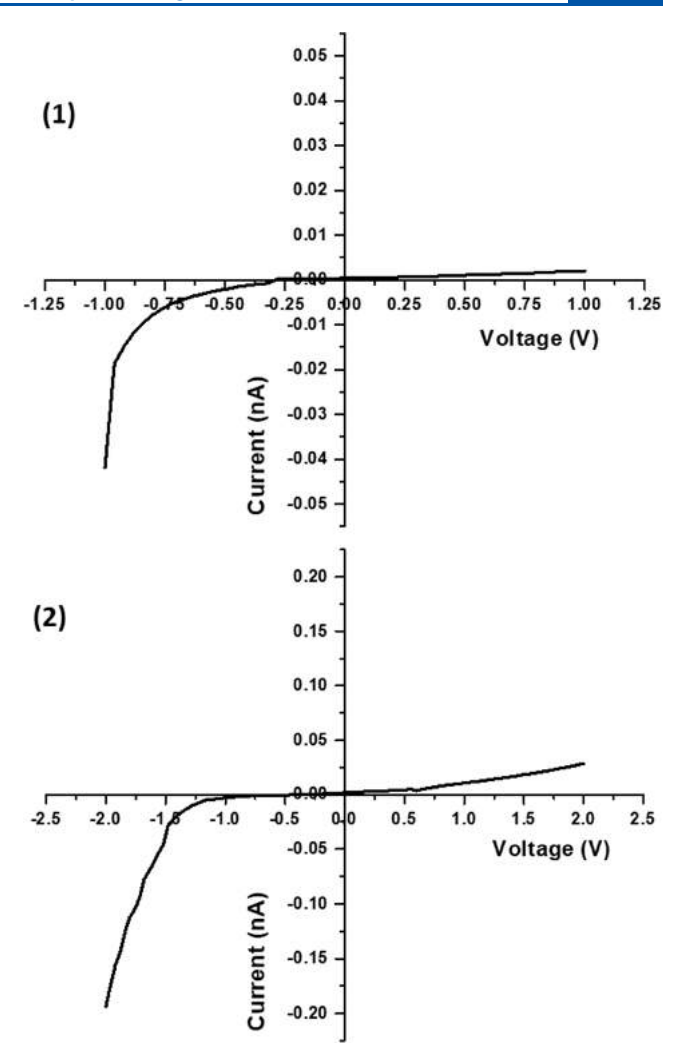


Figure 6. Characteristic current/voltage response observed for vanadyl-containing AulLB1|Au and chromium-containing AulLB2|Au junctions.

The higher the RR, the more precise the control of current.⁵ Species 1 showed RR values from 2.05 to 5.93 between -4 and +4 V, from 2.41 to 5.34 between -2 and +2 V and 2.18 to 19.90 between -1 and +1 V. Species 2 displayed RR values from 3.80 to 4.70 between +4 and -4 V, from 4.67 to 17.22 between +2 and -2 V, and 2.99 to 5.94 between +1 and -1 V. These values are comparable, although less pronounced than the published¹⁰ values for the iron-containing 3 that range from 3.99 to 28.6 between -2 and +2 V and from 2.04 to 31 between -4 and +4 V. Interestingly, the amplitude of the current signal is comparable for 1 and 2 but less pronounced than that of 3. This observation, allied with the fact that neither 1 nor 2 present well-defined metal reductions, led us to ponder on the similarities and differences in charge transfer mediated by 3d¹ V^{IV}O (1), 3d³ Cr^{III} (2), and 3d⁵ Fe^{III}. Additionally, we note that 1 and 3 adopt a square pyramidal geometry within an idealized $C_{4\nu}$ symmetry ($C_{2\nu}$ if N, O donors are considered), while 2 is pseudo-octahedral.

Feasibility and Verification of Electron Transport. Unidirectional electron transport or rectification through a molecular metallosurfactant requires that the solid-state potentials of its frontier molecular orbitals are compatible with that of the Fermi levels $(E_{\rm F})$ in the gold electrodes in any given ${\rm Au_1}|{\rm LB}|{\rm Au_2}|$ junction. Electrode ${\rm Au_1}|$ is the ground

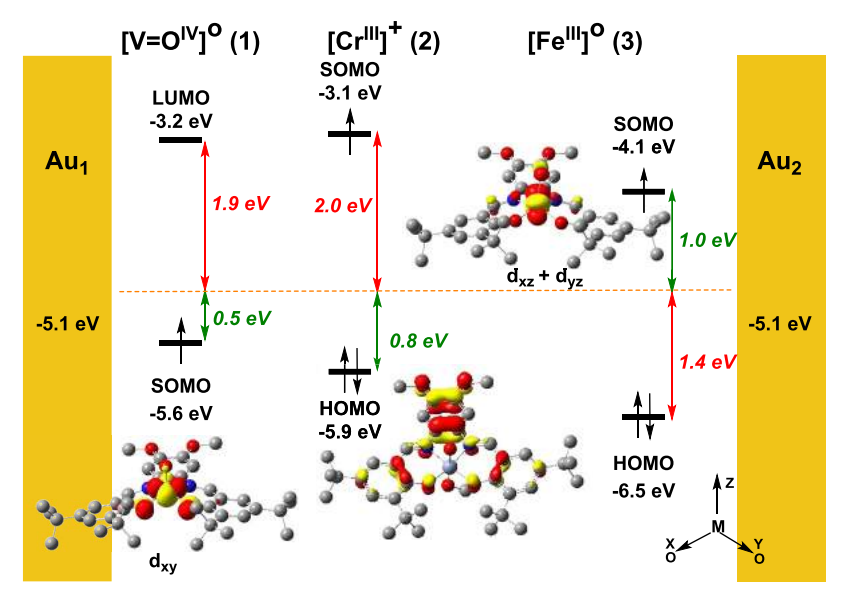


Figure 7. Comparison of frontier MO energy with Au electrode Fermi level for metallosurfactants 1, 2, and 3. MOs have an isodensity value of 0.05 a.u.

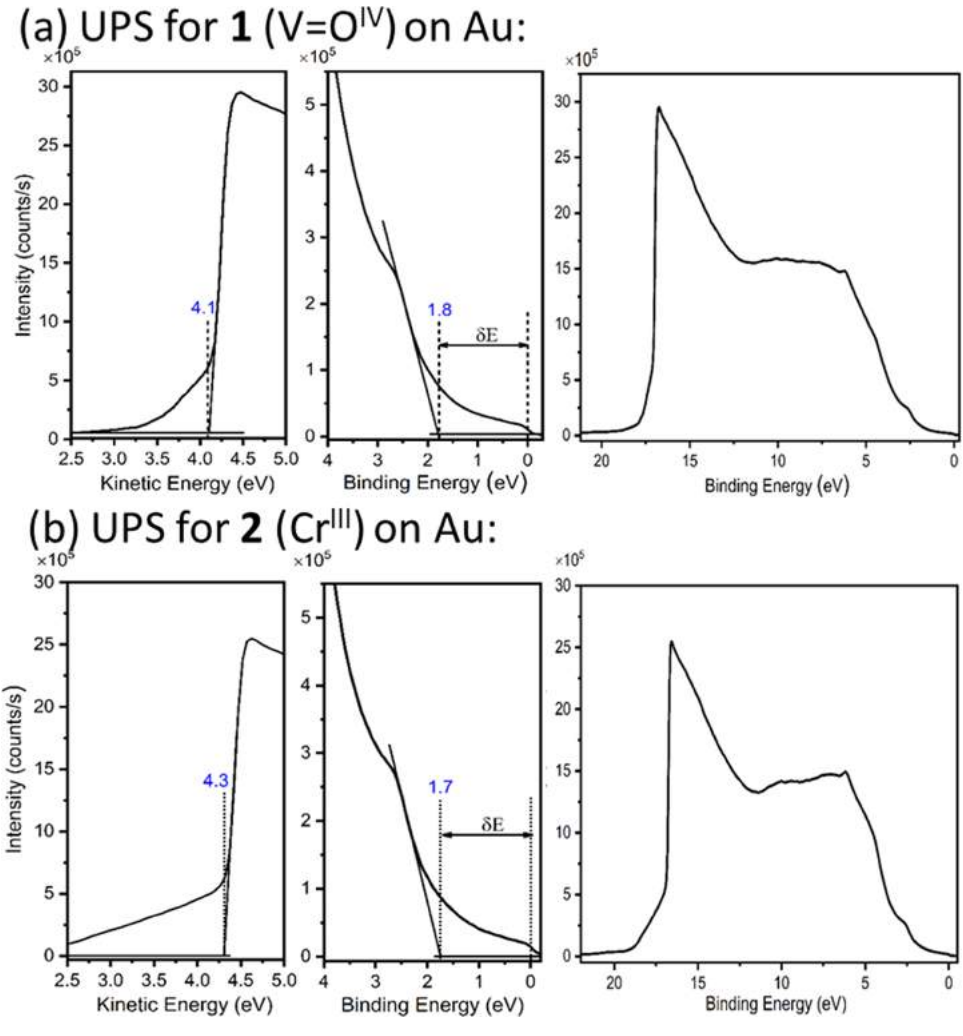


Figure 8. Secondary electron cutoff spectrum and the UPS spectrum of species 1 (V=O^{IV}) and 2 (Cr^{III}) deposited on a Au substrate.

substrate, and bias is applied to the top Au₂. Detailed surface analysis using IRRAS spectroelectrochemistry allows us to infer the position of the surfactant as asymmetrically located

between Au₁ and Au₂, and with the redox MOs closer to the top electrode.⁵² When a negative bias is applied to Au₂, its Fermi energy increases (*i.e.*, gets closer to zero), lifting the

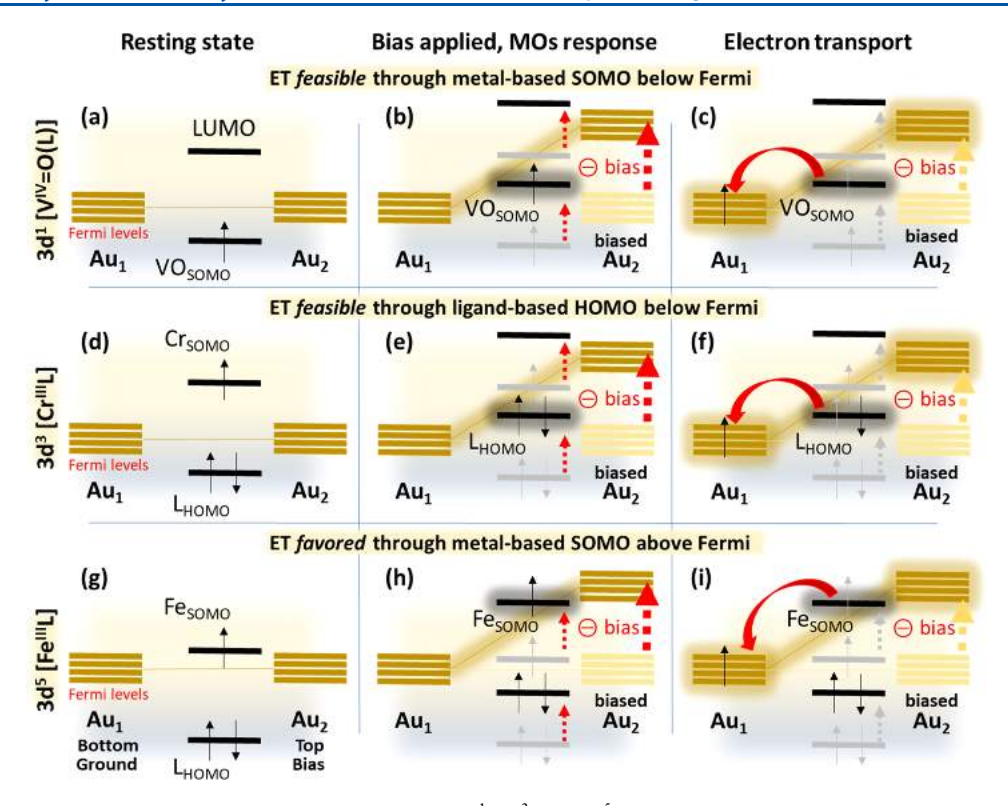


Figure 9. Individual stepwise mechanisms of electron transport for 3d¹, 3d³, and 3d⁵ metallosurfactants 1, 2, and 3. The figure displays the resting state, changes upon applying bias, and the first step in electron transport. An additional electron must be transported to replenish the initial state.

energies of the neighboring MOs. Although we cannot calculate with precision the energy of the biased Au_2 , we can obtain the MO energies from the experimental redox potentials given in V, according to the following equations

$$V_{\rm a} = 4.7 \text{ eV} + E_{1/2}^{\rm red}(\text{SCE})$$
 (1)

$$V_i = 4.7 \text{ eV} + (1.7)E_{1/2}^{\text{ox}}(\text{SCE})$$
 (2)

The V_a and V_i are approximately equal to the first electron affinity and first ionization energy levels of the molecule supported on the electrodes, respectively. $^{53-56}$ The $E_{1/2}^{\rm red}$ and $E_{1/2}^{\text{ox}}$ are the measured half-wave first reduction and first oxidation potentials, as referenced against the saturated calomel electrode (SCE). The processes appear, respectively, at $-1.47~V_{SCE}~(-1.88~V_{Fc+/Fc})$ and $+0.50~V_{SCE}~(+0.09~V_{Fc+/Fc})$ for the vanadyl-containing 1, and at -1.59 and +0.72 V_{SCE} $(-2.0 \text{ and } +0.31 \text{ V}_{\text{Ec+/Ec}})$ for the chromium-containing 2. For the V= O^{IV} containing 1, the V_i value correlates to the energy of a vanadyl-centered SOMO containing the 3d¹ electron and the V_a value correlates to the energy of the ligand-based LUMO. Using values of half-wave potentials, the solid-state energy of the metal-centered SOMO is calculated at -5.6 eV, and the energy of the LUMO is -3.2 eV. The metallosurfactant 2 displays the energy of the $3d^3\ Cr^{III}$ -based SOMO and of the phenylenediamine-based HOMO obtained from the V_a and V_i values, respectively, at -3.1 and -5.9 eV (Figure 7). These energies were further validated experimentally using ultraviolet photoelectron spectroscopy (UPS). The secondary electron cutoff and UPS spectrum observed for the LB films deposited on a gold substrate are shown in Figure 8a for 1 and Figure 8b for 2 with peaks at 1.8 and 1.7 eV, respectively. Therefore, the energies of the HOMO levels of the $V=O^{\dot{I}V}$ species 1 and the Cr^{III} species 2 were, respectively, calculated

as -5.9 and -6.0 eV in excellent agreement with the metalbased SOMO of 1 and the ligand-based HOMO of 2 calculated from cyclic voltammetric data and supported by DFT results. On the one hand, the SOMO of the $V=O^{IV}$ species 1 is approximately 0.5 eV below the Au Fermi level and is described by DFT methods as a 3d_{xv} orbital able to engage in electron transport. The LUMO is considerably mismatched at about 1.9 eV above the Fermi level (Figure 7). When bias is applied to the top electrode Au₂, the SOMO is lifted enabling transport through $Au_1 \leftarrow (3d_{xy}^{-1}) \leftarrow Au_2$. Consequently, the Cr^{III} species 2 must display a different transport mechanism, unlike the vanadyl 1, the metal-based SOMO shows a remarkable mismatch with the Au Fermi level. This is experimentally observed by the lack of a clear reduction wave for the CrIII/CrII couple. In the CrIII case, the HOMO is energetically closer to the Fermi level (~0.8 eV) than the SOMO that is 2.0 eV above. The forward bias applied to Au₂ lifts and aligns the ligand-based orbital, enabling transport Au₁ \leftarrow HOMO ($\uparrow\downarrow$), thus yielding a singly occupied MO (\uparrow or \downarrow) capable of receiving an electron from Au₂.

An overview of these findings appears in Figure 9, in which the $3d^1$ vanadyl species 1 has its singly populated metal-based SOMO lifted when bias is applied, enabling transport from A_2 into the metal-based $3d_{xy}^1$, and from there to Au_1 . The sequence of events, *i.e.*, whether $(3d_{xy}^1) \leftarrow Au_2$ or $Au_1 \leftarrow (3d_{xy}^1)$, is not clear at this point. These steps are summarized in Figure 9a–c. On the other hand, the energy of the metal-based SOMO in the $3d^3$ chromium species 2 is energetically mismatched with the Au Fermi levels, while the ligand-based HOMO is close to the Fermi level. We propose that upon an applied bias to A_2 , transport takes place from HOMO to A_1 . The resulting singly occupied MO can then receive an electron from Au_2 . This is summarized in Figure 9d–f. Both of these proposed electron transport pathways differ from that described for $3d^5$ iron-

based species 3^{10} and other Fe^{III} species with similar ligand environments^{57,58} in which the metal-centered SOMO is a linear combination of $d_{xz}+d_{yz}$ located ca. 1.0 eV above the Fermi level (Figure 7). In this case, $Au_1 \leftarrow SOMO \leftarrow Au_2$ transport is enabled (Figure 9g–i), and the fact that the SOMO is *above* the Fermi levels may lead to a better match once bias is applied, explaining the differences in current amplitude, where $1 \approx 2 < 3$. In each case, another electron must be transported to replenish the initial state. This step is not shown.

CONCLUSIONS

In conclusion, this study evaluated how 3d¹, 3d³, and HS3d⁵ electronic configurations influence the energies of SOMO and HOMO orbitals respective to the Fermi levels of gold electrodes in AulLBlAu junctions. The species $[V=O^{IV}L^{N_2O_2}]$ (1), $[Cr^{III}(L^{N_2O_2})(MeOH)(H_2O)]Cl(2)$, and $[Fe^{III}(L^{N_2O_2})Cl]$ (3) contain the same tetradentate ligand that confers comparable ligand fields and yields similar surface and film formation properties. Based on the interpretation of comprehensive electrochemical, spectroscopic, and microscopy methods allied to DFT calculations, we propose that directional electron transport in the previously published 3d5 Fe^{III} species takes place through the metal-based SOMOs (d_{xz} + d_{yz}) within 1 eV *above* the Fermi levels, while the 3d³ Cr^{III} species requires transport through ligand-based HOMOs 0.8 eV below the Fermi level. The 3d1 V=OIV species shows a mechanism based on the metal SOMO that is closer to that of HS3d⁵ Fe^{III} than to the *ligand-based* process seen for the 3d³ Cr^{III} species However, those orbitals are 0.5 eV below the Fermi level. These results verify our hypothesis that electron configuration is key to modulate MO/Fermi energies and point out the fact that conducting MOs below the Fermi level may be associated with a less pronounced current amplitude. These findings allow us to propose that the electronic configuration of the metal influences the selected tunneling pathway by which directional electron transfer takes place, and may bear relevance to the development of new molecular materials for spintronics.

ASSOCIATED CONTENT

Supporting Information

The Supporting Information is available free of charge at https://pubs.acs.org/doi/10.1021/acs.jpcc.2c04840.

Details of X-ray structural determination for species; UV—visible spectra for ligand, species and, and LB films; cyclic voltammograms; IRRAS spectra of LB films of and bulk IR spectra; ESI-MS spectra; AFM height images of monolayer films for and on mica substrates; *I–V* characteristics of and; DFT-calculated energetics of spin; and XYZ coordinates of DFT-calculated structures (PDF)

AUTHOR INFORMATION

Corresponding Authors

Shivnath Mazumder — Indian Institute of Technology, Jammu 181221, India; orcid.org/0000-0001-9166-8601; Email: shivnath.mazumder@iitjammu.ac.in

Cláudio N. Verani – Department of Chemistry, Wayne State University, Detroit, Michigan 48202, United States;

orcid.org/0000-0001-6482-1738; Email: claudio.verani@wayne.edu

Authors

A. D. K. Isuri Weeraratne — Department of Chemistry, Wayne State University, Detroit, Michigan 48202, United States; Present Address: Department of Chemistry, University of Sri Jayewardenepura, Nugegoda, 10250, Sri Lanka

Neha Rani — Indian Institute of Technology, Jammu 181221, India

Samudra Amunugama — Department of Chemistry, Wayne State University, Detroit, Michigan 48202, United States; Present Address: Intel, 2501 NW 229th Avenue, Hillsboro, Oregon 97124, United States

S. Sameera Perera – Department of Chemistry, Wayne State University, Detroit, Michigan 48202, United States

Kenneth K. Kpogo — Department of Chemistry, Wayne State University, Detroit, Michigan 48202, United States; Present Address: Moses Lake Industries, Moses Lake, Washington 98837, United States

Complete contact information is available at: https://pubs.acs.org/10.1021/acs.jpcc.2c04840

Author Contributions

A.D.K.I.W. and N.R. contributed equally to this work. A.D.K.I.W. contributed to investigation, formal analysis, methodology, and writing of original draft for syntheses, analysis, electrochemistry, film & junction fabrication, including IR reflectance absorbance and atomic force microscopy. N.R. contributed to investigation, formal analysis, methodology, and writing of original draft for DFT. S.A. contributed to investigation, formal analysis, and methodology for X-ray and UV photoelectron spectroscopy. S.S.P. contributed to investigation, formal analysis, and methodology for X-ray and UV photoelectron spectroscopy. K.K.K. contributed to investigation, formal analysis, and methodology for X-ray diffraction of single crystals. S.M. contributed to conceptualization, formal analysis, supervision, and writing (review & editing) of DFT section. C.N.V. contributed to overall conceptualization, data curation, formal analysis, funding acquisition, project administration, supervision, and writing (review & editing) of the manuscript.

Notes

The authors declare no competing financial interest.

ACKNOWLEDGMENTS

C.N.V. thankfully acknowledges support from the US National Science Foundation through grants NSF-CHE1904584 and NSF-CHE-1500201. S.M. acknowledges IIT Jammu for financial support toward computational workstations. A.D.K.I.W is a recipient of a Thomas C. Rumble Fellowship from the Graduate School at WSU and is partially supported by NSF. N.R. is supported by a DST INSPIRE award (IF180168) from the Department of Science and Technology, India. This work made use of the UPS/XPS facility that is partially funded by the National Science Foundation through grant NSF-MRI-1849578. The authors thank Dr. Izabella Brand, Universität Oldenburg, for a discussion on IRRAS surface selection rules, and acknowledge the Wayne State University Grid for additional computational resources.

REFERENCES

(1) Aviram, A.; Ratner, M. A. Molecular rectifiers. Chem. Phys. Lett. 1974, 29, 277-283.

- (2) Geddes, N.; Sambles, J.; Jarvis, D.; Parker, W.; Sandman, D. Fabrication and investigation of asymmetric current-voltage characteristics of a metal/Langmuir—Blodgett monolayer/metal structure. *Appl. Phys Lett.* **1990**, *56*, 1916—1918.
- (3) Ashwell, G. J.; Sambles, J. R.; Martin, A. S.; Parker, W. G.; Szablewski, M. Rectifying characteristics of Mgl($C_{16}H_{33}$ -Q3CNQ LB film)|Pt structures. *J. Chem. Soc. Chem. Commun.* **1990**, 19, 1374–1376.
- (4) Martin, A. S.; Sambles, J. R.; Ashwell, G. J. Molecular rectifier. *Phys. Rev. Lett.* **1993**, *70*, 218–221.
- (S) Metzger, R. M.; Chen, B.; Höpfner, U.; Lakshmikantham, M. V.; Vuillaume, D.; Kawai, T.; Wu, X.; Tachibana, H.; Hughes, T. V.; Sakurai, H.; Baldwin, J. W.; Hosch, C.; Cava, M. P.; Brehmer, L.; Ashwell, G. J. Unimolecular Electrical Rectification in Hexadecylquinolinium Tricyanoquinodimethanide. J. Am. Chem. Soc. 1997, 119, 10455—10466.
- (6) Ellenbogen, J. C.; Love, J. C. Architectures for molecular electronic computers. I. Logic structures and an adder designed from molecular electronic diodes. *Proc. IEEE* **2000**, *88*, 386–426.
- (7) Kornilovitch, P.; Bratkovsky, A.; Williams, R. S. Current rectification by molecules with asymmetric tunneling barriers. *Phys. Rev. B* **2002**, *66*, No. 165436.
- (8) Liu, R.; Ke, S.-H.; Yang, W.; Baranger, H. U. Organometallic molecular rectification. *J. Chem. Phys.* **2006**, *124*, No. 024718.
- (9) Wickramasinghe, L. D.; Perera, M. M.; Li, L.; Mao, G.; Zhou, Z.; Verani, C. N. Rectification in Nanoscale Devices Based on an Asymmetric Five-Coordinate Iron(III) Phenolate Complex. *Angew. Chem., Int. Ed.* **2013**, *52*, 13346–13350.
- (10) Wickramasinghe, L. D.; Mazumder, S.; Gonawala, S.; Perera, M. M.; Baydoun, H.; Thapa, B.; Li, L.; Xie, L.; Mao, G.; Zhou, Z.; Schlegel, H. B.; Verani, C. N. The Mechanisms of Rectification in Aul MoleculelAu Devices Based on Langmuir—Blodgett Monolayers of Iron(III) and Copper(II) Surfactants. *Angew. Chem., Int. Ed.* **2014**, *53*, 14462—14467.
- (11) Johnson, M. S.; Wickramasinghe, L.; Verani, C.; Metzger, R. M. Confirmation of the Rectifying Behavior in a Pentacoordinate $[N_2O_2]$ Iron (III) Surfactant Using a "Eutectic GaInl LB Monolayerl Au" Assembly. J. Phys. Chem. C **2016**, 120, 10578–10583.
- (12) Johnson, M. S.; Horton, C. L.; Gonawala, S.; Verani, C. N.; Metzger, R. M. Observation of current rectification by a new asymmetric iron (III) surfactant in a eutectic GaInl LB monolayerl Au sandwich. *Dalton Trans.* **2018**, *47*, 6344–6350.
- (13) Wolf, S. A.; Awschalom, D.; Buhrman, R.; Daughton, J.; von Molnár, vS.; Roukes, M.; Chtchelkanova, A. Y.; Treger, D. Spintronics: a spin-based electronics vision for the future. *Science* **2001**, 294, 1488–1495.
- (14) Jadaun, P.; Register, L. F.; Banerjee, S. K. Rational design principles for giant spin Hall effect in 5d-transition metal oxides. *Proc. Natl. Acad. Sci.* **2020**, *117*, 11878–11886.
- (15) Yuan, L.; Franco, C.; Crivillers, N.; Mas-Torrent, M.; Cao, L.; Sangeeth, C. S.; Rovira, C.; Veciana, J.; Nijhuis, C. A. Chemical control over the energy-level alignment in a two-terminal junction. *Nat. Commun.* **2016**, *7*, No. 12066.
- (16) Nijhuis, C. A.; Reus, W. F.; Whitesides, G. M. Mechanism of rectification in tunneling junctions based on molecules with asymmetric potential drops. *J. Am. Chem. Soc.* **2010**, *132*, 18386—18401.
- (17) Souto, M.; Yuan, L.; Morales, D. C.; Jiang, L.; Ratera, I.; Nijhuis, C. A.; Veciana, J. Tuning the rectification ratio by changing the electronic nature (open-shell and closed-shell) in donor—acceptor self-assembled monolayers. *J. Am. Chem. Soc.* **2017**, 139, 4262–4265.
- (18) Osorio, E. A.; Moth-Poulsen, K.; van der Zant, H. S. J.; Paaske, J.; Hedegård, P.; Flensberg, K.; Bendix, J.; Bjørnholm, T. Electrical Manipulation of Spin States in a Single Electrostatically Gated Transition-Metal Complex. *Nano Lett.* **2010**, *10*, 105–110.
- (19) Karuppannan, S. K.; Martín-Rodríguez, A.; Ruiz, E.; Harding, P.; Harding, D. J.; Yu, X.; Tadich, A.; Cowie, B.; Qif, D.; Nijhuis, C. A. Chem. Sci. 2021, 12, 2381.

- (20) APEX, I. Collection and Processing Programs are distributed by the Manufacturer; Bruker AXS Inc.: Madison, WI, USA, 2009.
- (21) Dolomanov, O. V.; Bourhis, L. J.; Gildea, R. J.; Howard, J. A.; Puschmann, H. OLEX2: a complete structure solution, refinement and analysis program. *J. Appl. Crystallogr.* **2009**, 42, 339–341.
- (22) Bourhis, L. J.; Dolomanov, O. V.; Gildea, R. J.; Howard, J. A.; Puschmann, H. The anatomy of a comprehensive constrained, restrained refinement program for the modern computing environment—Olex2 dissected. *Acta Crystallogr., Sect. A: Found. Adv.* **2015**, 71, 59—75.
- (23) Sheldrick, G. M. A short history of SHELX. Acta Crystallogr., Sect. A: Found. Crystallogr. 2008, 64, 112–122.
- (24) Calais, J. L. Density-Functional Theory of Atoms and Molecules; Parr, R. G.; Yang, W., Eds.; Oxford University Press: New York, Oxford, 1989.
- (25) Frisch, M. J.; Trucks, G. W.; Schlegel, H. B.; Scuseria, G. E.; Robb, M. A.; Cheeseman, J. R.; Scalmani, G.; Barone, V.; Mennucci, B.; Petersson, G. A.et al. *Gaussian 09*, revision A.1; Gaussian, Inc.: Wallingford, CT, 2009.
- (26) Vosko, S. H.; Wilk, L.; Nusair, M. Accurate spin-dependent electron liquid correlation energies for local spin density calculations: a critical analysis. *Can. J. Phys.* **1980**, *58*, 1200–1211.
- (27) Lee, C.; Yang, W.; Parr, R. G. Development of the Colle-Salvetti correlation-energy formula into a functional of the electron density. *Phys. Rev. B* **1988**, *37*, 785–789.
- (28) Andrae, D.; Haeussermann, U.; Dolg, M.; Stoll, H.; Preuss, H. Energy-adjusted ab initio pseudopotentials for the second and third row transition elements. *Theor. Chim. Acta* **1990**, *77*, 123–141.
- (29) Igel-Mann, G.; Stoll, H.; Preuss, H. Pseudopotentials for main group elements (IIIa through VIIa). *Mol. Phys.* **1988**, *65*, 1321–1328.
- (30) Dunning, T. H., Jr.; Hay, P. J. Modern Theoretical Chemistry. 1976.
- (31) Francl, M. M.; Pietro, W. J.; Hehre, W. J.; Binkley, J. S.; Gordon, M. S.; DeFrees, D. J.; Pople, J. A. Self-consistent molecular orbital methods. XXIII. A polarization-type basis set for second-row elements. *J. Chem. Phys* **1982**, *77*, 3654–3665.
- (32) Hariharan, P. C.; Pople, J. A. The influence of polarization functions on molecular orbital hydrogenation energies. *Theor. Chim. Acta* 1973, 28, 213–222.
- (33) Marenich, A. V.; Cramer, C. J.; Truhlar, D. G. Universal solvation model based on solute electron density and on a continuum model of the solvent defined by the bulk dielectric constant and atomic surface tensions. *J. Phys. Chem. B* **2009**, *113*, 6378–6396.
- (34) Dennington, R.; Keith, T.; Millam, J.; GaussView, V. Shawnee Mission KS, GaussView, Version; Semichem Inc. 2009.
- (35) Martinez, L. E.; Leighton, J. L.; Carsten, D. H.; Jacobsen, E. N. Highly Enantioselective Ring Opening of Epoxides Catalyzed by (salen)Cr(III) Complexes. J. Am. Chem. Soc. 1995, 117, 5897–5898.
- (36) Grivani, G.; Bruno, G.; Rudbari, H. A.; Khalaji, A. D.; Pourteimouri, P. Synthesis, characterization and crystal structure determination of a new oxovanadium(IV) Schiff base complex: The catalytic activity in the epoxidation of cyclooctene. *Inorg. Chem. Commun.* **2012**, *18*, 15–20.
- (37) Cuesta-Aluja, L.; Castilla, J.; Masdeu-Bulto, A. M. Aluminium salabza complexes for fixation of CO2 to organic carbonates. *Dalton Trans.* **2016**, *45*, 14658–14667.
- (38) Kochem, A.; Jarjayes, O.; Baptiste, B.; Philouze, C.; Vezin, H.; Tsukidate, K.; Tani, F.; Orio, M.; Shimazaki, Y.; Thomas, F. One-Electron Oxidized Copper (II) Salophen Complexes: Phenoxyl versus Diiminobenzene Radical Species. *Chem. Eur. J.* **2012**, *18*, 1068–1072.
- (39) Orio, M.; Jarjayes, O.; Kanso, H.; Philouze, C.; Neese, F.; Thomas, F. X-Ray Structures of Copper (II) and Nickel (II) Radical Salen Complexes: The Preference of Galactose Oxidase for Copper (II). *Angew. Chem.* **2010**, *122*, 5109–5112.
- (40) Liu, Z.; Anson, F. C. Electrochemical properties of vanadium (III, IV, V)— salen complexes in acetonitrile. Four-electron reduction of O2 by V (III)— salen. *Inorg. Chem.* **2000**, 39, 274—280.

- (41) The addition of the name Pockels to the films commonly referred to as Langmuir monolayers aims to address a historical omission toward the pioneering work of Agnes Pockels (1862–1935) in the understanding of film formation at the air—water interface. See the following references: (a) Rayleigh, L.; Pockels, A. Surface tension. *Nature* 1891, 43, 437–439. (b) Pockels, A. On the relative contamination of the water-surface by equal quantities of different substances. *Nature* 1892, 46, 418–419. (c) Pockels, A. Relations between the surface-tension and relative contamination of water surfaces. *Nature* 1893, 48, 152–154. (d) Pockels, A. On the spreading of oil upon water. *Nature* 1894, 50, 223–224.
- (42) Shakya, R.; Hindo, S. S.; Wu, L.; Allard, M. M.; Heeg, M. J.; Hratchian, H. P.; McGarvey, B. R.; da Rocha, S. R. P.; Verani, C. N. Archetypical Modeling and Amphiphilic Behavior of Cobalt(II)-Containing Soft-Materials with Asymmetric Tridentate Ligands. *Inorg. Chem.* 2007, 46, 9808–9818.
- (43) Ries, H. E., Jr. Stable ridges in a collapsing monolayer. *Nature* 1979, 281, 287.
- (44) Mitsuishi, M.; Zhao, F.; Kim, Y.; Watanabe, A.; Miyashita, T. Preparation of ultrathin silsesquioxane nanofilms via polymer Langmuir—Blodgett films. *Chem. Matter* **2008**, *20*, 4310–4316.
- (45) The intensity of an IR absorption mode is given by $\int Adv \cong \Gamma |\mu|^2 \langle \vec{E} \rangle^2 \cos^2\theta$, where A is the absorbance, d is the film thickness and v is the wavelength, Γ is the surface concentration of the adsorbed species, θ is the angle between the transition dipole moment vector $\vec{\mu}$ and the electric field vector \vec{E} of the p-polarized light. Therefore, this equation predicts that depending on the orientation of some functional groups in a molecular film, their IR absorption bands may be either enhanced or not detectable in the PM IRRA spectrum. When $(\vec{\mu}) \parallel \vec{E}$ the signal is enhanced and when $(\vec{\mu}) \perp \vec{E}$ the signal is not detected. In the case of metallosurfactant 1 the V=O group is perpendicular to the gold electrode, therefore justifying the absence of signal. For an authoritative discussion of IRRAS surface selection rules, see I. Brand, Application of Polarization Modulation Infrared Reflection Absorption Spectroscopy in Electrochemistry, Springer Nature Switzerland, 2020, pp. 26-41.
- (46) Verani, C. N.; Shanmugam, R.; Xavier, F. R.; Allard, M. M.; Kpogo, K. K. Electronic and interfacial behavior of gemini metallosurfactants with copper (II)/pseudohalide cascade cores. *Dalton Trans.* **2013**, 42, 15296–15306.
- (47) Yamamoto, Y.; Toyota, E. Paramagnetic cobalt (III) complexes with organic ligands. IX. the preparation and properties of paramagnetic tetraammine (5-nitrosalicylideneaminato) cobalt (III) complexes. *Bull. Chem. Soc. Jpn.* **1986**, *59*, 617–620.
- (48) Sawatzky, G. A.; Post, D. X-ray photoelectron and Auger spectroscopy study of some vanadium oxides. *Phys. Rev. B* **1979**, *20*, 1546–1555.
- (49) Moffat, T. P.; Latanision, R. An electrochemical and X-Ray photoelectron spectroscopy study of the passive state of chromium. *J. Electrochem. Soc.* **1992**, *139*, 1869–1879.
- (50) Metzger, R. M. Unimolecular electronics. *J. Mater. Chem.* **2008**, 18, 4364–4396.
- (51) Verani, C. N. Molecular rectifiers based on five-coordinate iron(III)-containing surfactants. *Dalton Trans.* **2018**, 47, 14153–14168
- (52) Brand, I.; Juhaniewicz-Debinska, J.; Wickramasinghe, L.; Verani, C. N. An in situ spectroelectrochemical study on the orientation changes of an [Fe^{III}L^{N2O3}] metallosurfactant deposited as LB Films on gold electrode surfaces. *Dalton Trans.* **2018**, 47, 14218–14226.
- (53) He, J.; Fu, Q.; Lindsay, S.; Ciszek, J. W.; Tour, J. M. Electrochemical origin of voltage-controlled molecular conductance switching. *J. Am. Chem. Soc.* **2006**, *128*, 14828–14835.
- (54) Hipps, K. Scanning Tunneling Spectroscopy (STS). In Handbook of Applied Solid State Spectroscopy; Springer, 2006; pp 305–350.
- (55) Scudiero, L.; Barlow, D. E.; Hipps, K. Scanning tunneling microscopy, orbital-mediated tunneling spectroscopy, and ultraviolet

- photoelectron spectroscopy of nickel (II) octaethylporphyrin deposited from vapor. J. Phys. Chem. B 2002, 106, 996–1003.
- (56) Schmidt, A.; Armstrong, N.; Goeltner, C.; Muellen, K. Electronic structure of oligorylenes in thin solid films. *J. Phys. Chem. A* **1994**, *98*, 11780–11785.
- (57) Weeraratne, A. D. K. I.; Baydoun, H.; Shakya, R.; Niklas, J.; Xie, L.; Mao, G.; Stoian, S. A.; Poluektov, O. G.; Verani, C. N. Observation of current rectification by the new bimetallic iron(iii) hydrophobe $[\text{Fe}_2^{\text{III}}(L^{N_4O_6})]$ on AulLB-moleculelAu devices. *Dalton Trans.* **2018**, 47, 14352–14361.
- (58) Wickramasinghe, L. D.; Mazumder, S.; Kpogo, K. K.; Staples, R. J.; Schlegel, H. B.; Verani, C. N. Electronic Modulation of the SOMO–HOMO Energy Gap in Iron(III) Complexes towards Unimolecular Current Rectification. *Chem. Eur. J.* **2016**, *22*, 10786–10790.